Optik 135 (2017) 190–199

Contents lists available at ScienceDirect

Optik

journal homepage: www.elsevier.de/ijleo

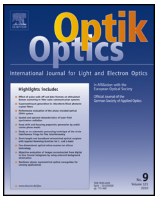

Original research article

Effect of Cd^{2+} concentration on $ZnFe_2O_4$ nanoparticles on the structural, optical and magnetic properties

K. Kombaiah[a], J. Judith Vijaya[a,*], L. John Kennedy[b], M. Bououdina[c], K. Kaviyarasu[d,e], R. Jothi Ramalingam[f], Murugan A. Munusamy[g], Abulla AlArfaj[g]

[a] *Catalysis and Nanomaterials Research Laboratory, Department of Chemistry, Loyola College (Autonomous), Chennai-34, India*
[b] *Materials Division, School of Advanced Sciences, Vellore Institute of Technology (VIT) University, Chennai Campus, Chennai-127, India*
[c] *Department of Physics, College of Science, University of Bahrain, PO Box 32038, Bahrain*
[d] *UNESCO-UNISA Africa Chair in Nanosciences/Nanotechnology Laboratories, College of Graduate Studies, University of South Africa (UNISA), Muckleneuk Ridge, P O Box 392, Pretoria, South Africa*
[e] *Nanosciences African Network (NANOAFNET), Materials Research Department (MSD), iThemba LABS-National Research Foundation (NRF), 1 Old Faure Road, 7129, P O Box 722 Box 722, Somerset West, Western Cape Province, South Africa*
[f] *Surfactant Research Chair, Chemistry Department, College of Science, King Saud University, Riyadh 11451, Saudi Arabia*
[g] *Department of Botany and Microbiology, College of Science, King Saud University, Riyadh 11451, Saudi Arabia*

ARTICLE INFO

Article history:
Received 30 November 2016
Received in revised form 23 January 2017
Accepted 24 January 2017

Keywords:
Crystal morphology
Optical microscopy
Surface structure
Microwave
Nanomaterials
VSM

ABSTRACT

Simple, cost effective and low temperature synthesis of pure and Cd^{2+} doped zinc ferrite nanoparticles have been successfully synthesized by a microwave assisted combustion method using metal nitrates as oxidizing agent and L-arginine as a reducing agent. The stoichiometric ratio of precursors taken was 1:2. X-ray diffraction, Rietveld, FTIR, HRSEM, DRS, PL, and VSM techniques are carried out to characterize the samples for the structural phases, functional groups, morphology, optical and magnetic properties. Upon the combustion method, the crystallinity and size variation of the nanoparticles were decreased from 42 nm to 12 nm with increasing the concentration of the dopant. The lattice parameter of the spinel structure increases when the size of the nanoparticles reduced. FTIR spectra confirmed the presence of metal oxides absorption bands at lower and higher frequency regimes, due to tetrahedral, and octahedral stretching vibrations respectively. HRSEM images showed the presence of spherical particles in the nano-regime. The bandgap energy of the samples was estimated by diffuse reflectance spectra and it decreased with increasing dopant concentration which was calculated from Tauc's relation. Photoluminescence (PL) spectroscopy used to investigate the emission of the samples with the excitation wavelength at 414 nm and emission at 486 nm. Vibrating sample magnetometer under applied magnetic field was used to carry out the magnetic measurements and it revealed at decrease in saturation magnetization and an increase in coercivity with an increase in the concentration of Cd^{2+} ions. The microwave combustion method produces the ferrite nanoparticles as clean, non-toxic, environment-friendly with high yield of product in a shorter reaction time. The future plan of this research is to synthesize highly active catalyst for the photocatalytic mineralization of industrial effluent in large scale.

---

* Corresponding author.
E-mail addresses: jjvijayaloyola@yahoo.co.in, jjvijaya78@gmail.com (J.J. Vijaya).

http://dx.doi.org/10.1016/j.ijleo.2017.01.066
0030-4026/

1. Introduction

Currently studies on nanocrystalline magnetic materials have become important in research community. As novel materials, they have attracted considerable interest on account of their optical, electrical, electronic, magnetic and catalytic properties [1–5]. Because of their extensive magnetic properties, the ferrite nanoparticles are involved in a large number of applications, such as, magnetic media [6,7], microwave [8,9], gas sensors [10,11], ferrofluids [12,13] and transformer cores [14,15]. The spinel ferrites have the general formula MFe_2O_4, where, M- stands for metal cations like Co, Zn, Cu, Ni, etc. In these materials, by doping the third metal ion into the spinel structure, some of the ions are replaced by the third metal and the distribution of ions can be easily altered, which leads to the changes in the properties of the nanomaterials [16]. The effect on the magnetization depends on the site preferred by the substituents. Various parameters, such as, saturation magnetization, coercivity, remanant magnetization, and permittivity play an important role to identify the magnetic properties of the materials [17]. The properties of spinel ferrite magnetic materials depend mainly on the super exchange interaction between the metal cations in the tetrahedral and octahedral sites [18]. In the past few years, various methods have been used to synthesize nanocrystalline materials, such as, co-precipitation, ball milling, conventional method, mechanical milling and combustion method [19–21]. Among these, the combustion method is the most efficient one compared to other methods. When assisted by microwave, it is known as microwave assisted combustion method. A simple, cost effective, non-toxic and quick way to synthesize metal nanoparticles using microwave assisted combustion method leads to high quality and better yield of the products. The crystallite size, particle size, bandgap energy, magnetization and magnetic coercivity of the nanoparticles processed by this method are affected by varying the concentration of the dopant [22]. By changing the parameters, such as, temperature, pH, complexing agent, and solvent polarity, one can optimize the magnetic properties. The fuel plays an essential role in the enhanced efficiency of the reaction. For example, organic compounds, such as, glycine, urea, citric acid, alanine, and L-arginine was used as fuels [23]. When the fuel is used along with the metal nitrates, it leads to the formation of nano-regime particles, due to the exothermic reaction that takes place between the oxidant and fuel, during the microwave radiation [24]. The mechanism involved in microwave heating method is completely different from the one involved in conventional heating. In microwave, the material is uniformly heated on a molecular level. The heat generated inside the microwave oven is governed by the dipole moment of the molecules. Therefore, the homogeneous heat is generated inside the solution, which is contained in a silica crucible, and the reaction results in the enormous evolution of fumes. Finally, the nanostructured materials are formed within few minutes of the process [25].

Nanoparticles play an integral role and have found potential applications in various streams of nanotechnology. The problem of waste disposal and pollution due to rice husk has been solved by the synthesis of nano silica. Silica in the amorphous form constitutes 87–97% of combustion product from the rice husk. Conversion of silica nanoparticles to nanosilica has been successful and highly applicative [26]. Granular magnetic materials due to its high degree of electronic spin polarization are found to be applicative in the field of sensors. Ferromagnetic magnetite powders synthesized by arc-discharge method in a partial oxygen atmosphere exhibits high intergrain spin- dependant tunneling magneto resistance [5]. Nanoparticles also exhibit unique electrical and optical properties. Kaviyarasan et al., have succeeded in preparing PbI_2 nanorods of one dimension (1D) without implying any surfactant and capping agents [27]. Similarly, Cds (1D) nanocrystals were synthesized by a simple hydrothermal route without using any capping agent [28]. The same method has been implied to obtain a highly ordered MgO. AgO nanocube arrays finding its way in the field of optoelectronics [29]. CdO nanofibres (1D) have been synthesized by a solvothermal method. This belongs to the family of transparent conducting oxides suitable for light emitting diodes, anti reflection coatings, chemical sensors, and solar cells etc [30]. A two-step hydrothermal synthesis was carried out to prepare CuSe quantum dots. These nanoparticles have good photocatalytic property for the dehydration of environmental benign dye Rhodamine-B [31]. Nickel oxide nanorods prepared through sol-gel method exhibits excellent solar cell efficiency [32]. The aim of the present study is the enhancement of structural, optical and magnetic properties of $ZnFe_2O_4$ nanoparticles prepared with and without Cd^{2+} doping. Though, there is a literature found on CdO-$ZnFe_2O_4$ composites prepared by the precipitation method [33], we have used microwave combustion method in the present study, which yields the products within shorter time than the reported one. The effect of Cd^{2+} dopant on the structural, optical and magnetic properties is discussed using XRD, Rietveld, HR-SEM, EDX, DRS, PL, and VSM studies.

2. Experimental section

2.1. Preparation of $Cd_xZn_{1-x}Fe_2O_4$ nanoparticles

The chemical reagents utilized in our investigation are of analytical grade and used as such without additional purification. The precursors are zinc nitrate [$Zn(NO_3)_2$. $6H_2O$], ferric nitrate [$Fe(NO_3)_3 \cdot 9H_2O$] and cadmium nitrate [$Cd(NO_3)_2 \cdot 4H_2O$] and they are taken in the respective stoichiometric amounts and fuel used is l-arginine [$C_6H_{14}N_4O_2$]. Different molar ratio of cadmium doped $Cd_xZn_{1-x}Fe_2O_4$ nanoparticles ($x = 0.0, 0.1, 0.2, 0.3, 0.4, 0.5$) were prepared. They were dissolved separately in 10 mL of distilled water using magnetic stirrer. The separately dissolved precursors were mixed together and stirred with a magnetic stirrer for an hour to obtain a clear homogeneous solution. The obtained clear solutions were then poured into a silica crucible and placed in a microwave oven for 10 min at 850 W output power, and frequency 2.54 GHz. In the beginning, dehydration took place due to the solution boiling, and then the spontaneous combustion was reached within a few minutes

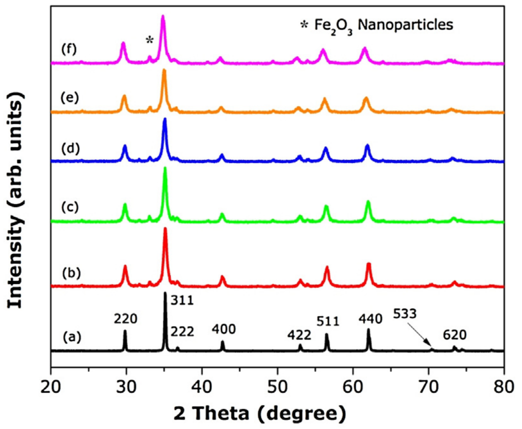

Fig. 1. XRD pattern of (a) Pure $ZnFe_2O_4$, (b) $Cd_{0.1}Zn_{0.9}Fe_2O_4$, (c) $Cd_{0.2}Zn_{0.8}Fe_2O_4$, (d) $Cd_{0.3}Zn_{0.7}Fe_2O_4$, (e) $Cd_{0.4}Zn_{0.6}Fe_2O_4$, (f) $Cd_{0.5}Zn_{0.5}Fe_2O_4$ cubic nanoparticles.

Table 1
Structural and lattice parameter values of pure and Cd^{2+} doped $ZnFe_2O_4$ nanoparticles.

Sample	Crystallite Size (nm)	Strain (%)	Lattice Parameters (Å)	Fit Parameters
Pure $ZnFe_2O_4$	42	0.073	8.4434	R_{wp} 12.73% S 1.05
$Cd_{0.1}Zn_{0.9}Fe_2O_4$	37	0.008	8.448	R_{wp} 17.47% S 1.11
$Cd_{0.2}Zn_{0.8}Fe_2O_4$	24	0.110	8.4587	R_{wp} 20.39% S 1.19
$Cd_{0.3}Zn_{0.7}Fe_2O_4$	19	0.175	8.479	R_{wp} 23.47% S 1.26
$Cd_{0.4}Zn_{0.6}Fe_2O_4$	15	0.440	8.493	R_{wp} 27.30% S 1.31
$Cd_{0.5}Zn_{0.5}Fe_2O_4$	12	0.500	8.512	R_{wp} 31.38% S 1.37

followed by the release of heat by burning and the solution vaporized instantly. At the end of the reaction powder obtained is washed with ethanol and finally dried in a hot air oven at 100 °C for 1 h.

2.2. Characterization technique

The formation of structural phases is confirmed by using Rigaku Ultima IV high resolution X-ray diffractometer (XRD) using CuKα radiation at $\lambda = 0.154$ nm. Since there is no XRD peaks observed in the range of 0–20°, the XRD pattern is recorded from 20 to 80° (2θ) in the present study. Rietveld method is used to refine further using the PDXL programme. Perkin Elmer infrared spectrophotometer (model RX l) is used in the range of 4000 cm^{-1}–400 cm^{-1} to identify the functional groups. The formation of nanoparticles is confirmed by HRSEM analysis using a Joel JSM6360. Cary100 UV–vis spectrophotometer is used to calculate the band gap energy of the samples and Varian Cary Eclipse Fluorescence spectrophotometer is used to study the emission properties of the nanoparticles. PMC MicroMag3900 model vibrating sample magnetometer (VSM) equipped with 1T magnet is used to identify the magnetic properties of the samples at room temperature.

3. Results and discussion

3.1. XRD analysis

Fig. 1(a–f) depicts the X-ray diffraction of the as-prepared Cd^{2+} doped $ZnFe_2O_4$ nanoparticles ($Cd_xZn_{1-x}Fe_2O_4$) with different x values (x = 0.0, 0.1, 0.2, 0.3, 0.4, 0.5) and compared with the ones prepared without any additional dopant. After analyzing the XRD studies of all the samples, the reflecting planes (220), (311), (222), (400), (422), (511), (440), (620), (533), (622) and (444) confirm the formation of single phase cubic spinel structure for pure $ZnFe_2O_4$ sample. It represents the solubility of cations into their corresponding lattice sites. The (*hkl*) indices help us to identify the phase purity of the samples. Comparing the peaks of the pure $ZnFe_2O_4$ sample with that of the Cd^{2+} doped $Zn_{1-x}Fe_2O_4$ samples, some additional peaks are found to be formed with the variation of dopant values. The presence of one additional peak in the doped samples implies the presence of trace amount of α-Fe_2O_3 phase as an impurity in the sample and it corresponds to α-Fe_2O_3 phase (JCPDS file no-89-0597). The peak obtained at $2\theta = 33.09°$ corresponds to (104) plane of α-Fe_2O_3 phase, and the values of $ZnFe_2O_4$ XRD peaks corresponds to the JCPDS Card No: 89-4926. The average crystallite sizes of the samples were calculated by measuring the (FWHM) of the most intense peak (311) plane, by using Scherrer equation [34]. The average crystallite size of the samples estimated from the Scherrer equation is listed in Table 1. It has been observed that the crystallite size decreased from 42 to 12 nm with an increase in the Cd^{2+} content. The similar result seen in other cases [35,36].

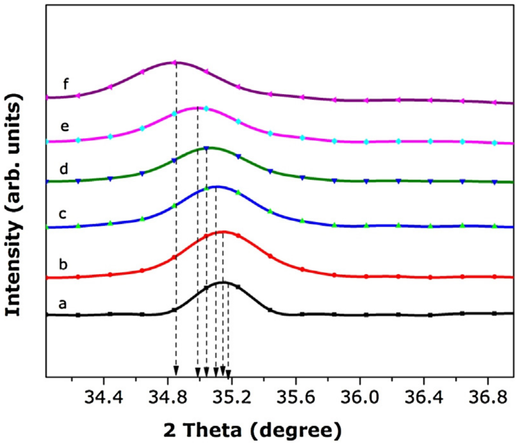

Fig. 2. Variation the XRD patterns of (a) Pure $ZnFe_2O_4$, (b) $Cd_{0.1}Zn_{0.9}Fe_2O_4$, (c) $Cd_{0.2}Zn_{0.8}Fe_2O_4$, (d) $Cd_{0.3}Zn_{0.7}Fe_2O_4$, (e) $Cd_{0.4}Zn_{0.6}Fe_2O_4$, (f) $Cd_{0.5}Zn_{0.5}Fe_2O_4$ nanoparticles in (311) plane.

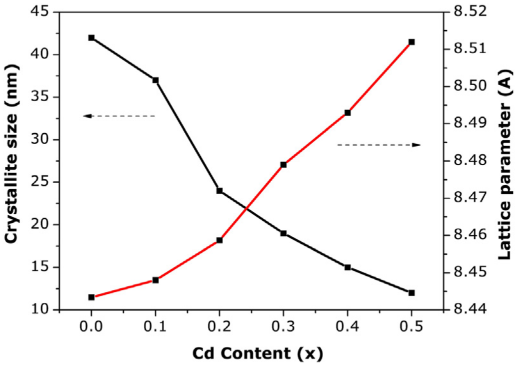

Fig. 3. Decreased pattern of crystallite size and increased pattern of lattice parameter of (a) Pure $ZnFe_2O_4$, (b) $Cd_{0.1}Zn_{0.9}Fe_2O_4$, (c) $Cd_{0.2}Zn_{0.8}Fe_2O_4$, (d) $Cd_{0.3}Zn_{0.7}Fe_2O_4$, (e) $Cd_{0.4}Zn_{0.6}Fe_2O_4$, (f) $Cd_{0.5}Zn_{0.5}Fe_2O_4$ nanoparticles.

Fig. 2 indicates an interesting observation that with an increase in the value of the dopant, the diffraction peaks are shifted and the increased broadening of the peak. Similar results have been reported in the literature [37,38]. This slight shift may be attributed to the higher ionic radius of the dopant ($Cd^{2+} = 0.97$ Å) in comparison to the pure sample ($Zn^{2+} = 0.74$ Å). The increase in microstrain causes small changes in 2θ values and peak broadening which in turn leads to the decrease in the size of the nanoparticles [39,40]. In this study, the lattice parameters of the synthesized sample have been calculated utilizing the respective (*h*, *k*, *l*) parameter and the d-spacing values.

$$\sin^2\theta = \frac{\lambda^2}{4}\left[\frac{4}{3}\left(\frac{h^2+hk+k^2}{a^2}\right)+\frac{l^2}{c^2}\right] \tag{1}$$

where λ is the wavelength of X-ray used (1.5402 Å), θ, the Bragg angle, a and c, lattice constants, and h, k, l are Miller indices. The lattice parameters of each composition was carried out from the above equation and listed out in Table 1. It was described that the value of lattice parameter for each composition found to be increase with an increase in Cd^{2+} content, which complies with Vegards's law [41]. This incrementation can be attributed to the size difference of the cations, since the unit cell expands, when the superseded cation size is more immense and the supersession of more minuscule cations Zn^{2+} (0.064 nm) by more immensely colossal cations Cd^{2+} (0.097 nm) [42]. Fig. 3 indicates that the fact with an increase in Cd^{2+} concentration, the lattice parameter increases and the average crystallite size decreases. Similar results are already reported [43,44].

3.2. Rietveld refinement analysis

The XRD pattern for all the samples were refined by Rietveld analysis. The analogous spectra observed portrait and the difference between the observed and refined portrait are plotted in Fig. 4. It is a powerful method to determine simultaneously the structural properties like crystallite size and microstructural parameters, such as, lattice parameter and lattice strain. Structural parameters and the refinement factors (S, R_{wp}) are tabulated in Table 1. Blue solid line curve shows the estimated

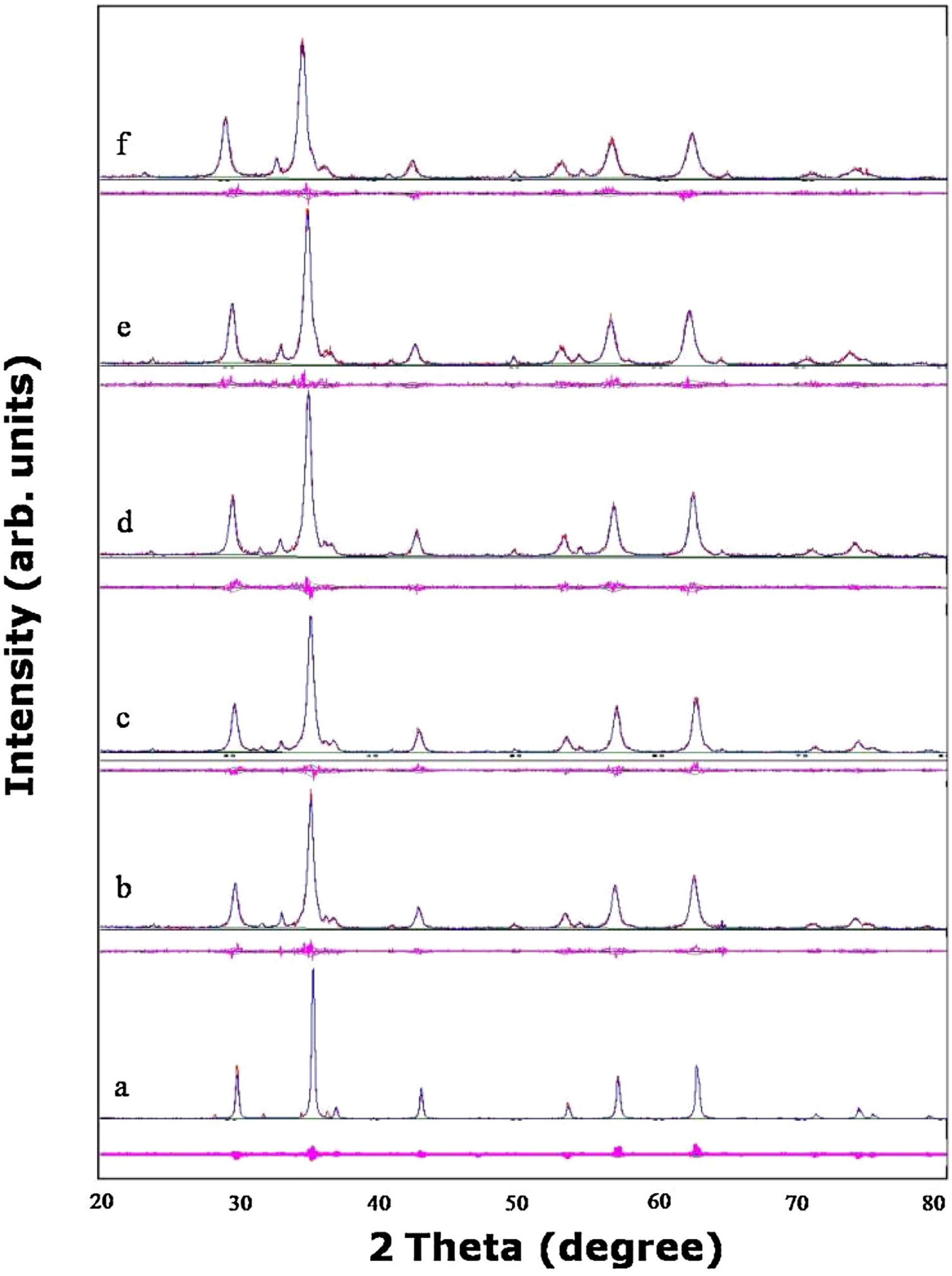

Fig. 4. Rietveld refinement of (a) Pure $ZnFe_2O_4$, (b) $Cd_{0.1}Zn_{0.9}Fe_2O_4$, (c) $Cd_{0.2}Zn_{0.8}Fe_2O_4$, (d) $Cd_{0.3}Zn_{0.7}Fe_2O_4$, (e) $Cd_{0.4}Zn_{0.6}Fe_2O_4$, (f) $Cd_{0.5}Zn_{0.5}Fe_2O_4$ nanoparticles.

patterns. The bottom line exhibits the discrepancy between the measured and reckoned intensities. Lattice parameter and crystallite size are influenced in grateful by the preparation technique, molar proportion of the selected precursors and the nature of precursor. The parameters refined were background, profile half-width parameters (u, v, w), thermal parameters, multiplier, zero shifting, lattice constants and atomic point parameters [45]. It can be seen that the refinements result in the fulfilled reliability factors and led to a satisfactory agreement acquired between the observed and computed patterns [46]. During the refinements, the quality of fit was quantified by the corresponding reliability factor $S = R_{wp}/R_e$, where R_{wp} and R_e, are, respectively, the R-weighted and the R-expected patterns [47]. The decreases in the peak position shifted towards lower angles and it showed the incrementation in the lattice parameters obtained from Rietveld refinement. The lattice parameter of pure $ZnFe_2O_4$ is found to be 8.4434 Å, which is good in agreement with the standard JCPDS value of 8.441 Å (JCPDS No. 22-1012). Also, the linear change in the value of lattice parameters is due to the change in the ionic radii of the replaced ions [48]. After the doping of Cd^{2+} ion, the values of lattice parameters and fit parameters (Table 1) are found to be increased.

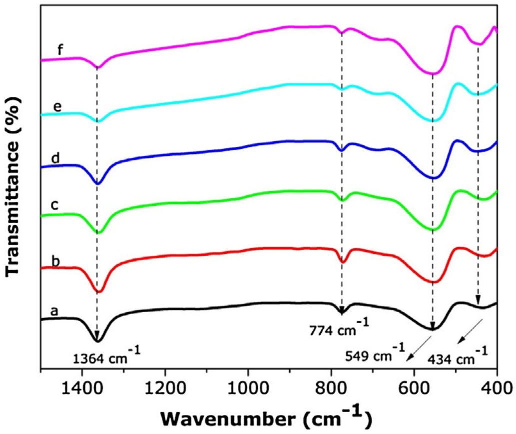

Fig. 5. Functional group analysis of (a) Pure $ZnFe_2O_4$, (b) $Cd_{0.1}Zn_{0.9}Fe_2O_4$, (c) $Cd_{0.2}Zn_{0.8}Fe_2O_4$, (d) $Cd_{0.3}Zn_{0.7}Fe_2O_4$, (e) $Cd_{0.4}Zn_{0.6}Fe_2O_4$, (f) $Cd_{0.5}Zn_{0.5}Fe_2O_4$ nanoparticles by using FTIR spectrum.

This may be ascribed to the differences in the ionic radii of Cd^{2+}, Zn^{2+}, and redistribution of Zn^{2+}, Fe^{3+} by Cd^{2+} within the tetrahedral/octahedral ionic sites [49].

3.3. Fourier transform-infrared spectroscopy studies

The vibrational frequencies of the as-prepared pure and doped zinc ferrite nanoparticles were analyzed by using FTIR spectra. All the results obtained at room temperature as shown in Fig. 5. The FT-IR spectra of pure and doped samples exhibit four major peaks. The main absorption peak around 549 cm^{-1} corresponds to the metal oxygen bands (M_{tet}—O) in tetrahedral sites [37,38]. Another peak around 434 cm^{-1} is attributed to the metal oxygen band (M_{oct}—O) with octahedral sites. The peak which appears at 774 cm^{-1} is assigned to metal-oxygen-metal (Zn—O—Fe) bands [50]. The band observed at 1364 cm^{-1} is ascribed to the stretching vibrations of O—H bond, which may be due to the absorption of water [51] during the preparation of the sample with KBr.

3.4. HRSEM analysis

The morphological studies of the as-prepared samples are examined by using high resolution scanning electron microscopy (HRSEM) and are shown in Fig. 6(a–f). Microstructure analysis provides information related to the average particle size and nature of grain growth, which in turn the magnetic and electrical properties of materials. The samples prepared by using microwave combustion method with different concentration ($x = 0.0, 0.1, 0.2, 0.3, 0.4, 0.5$) exhibit uniform and spherical shape. In Fig. 6a, the particles are tiny in size and they were tightly bound as the agglomerated form of nanoparticles. But, Fig. 6f shows that the particles that are bigger in size and loosely bounded. The increase in the particle size is due to the Cd^{2+} ions that occupies the grain boundary or octahedral sites. Since, the Cd^{2+} ion has larger ionic radius than Fe^{3+} ions, it may not be possible to occupy the tetrahedral sites. The occupancy of Cd^{2+} ions in the octahedral sites may increase the particle size of the nanoparticles. The mild growth of the dopant content makes the surface denser and decreases the crystallinity and particle size. Hence, surface morphology of the samples depends upon the nature of the precursor, dopant concentration and method of preparation.

3.5. UV–vis spectra and optical band gap studies

Fig. 7 shows the UV–vis reflectance spectra of $ZnFe_2O_4$ nanoparticles prepared with and without dopant. One of the most consequential optical parameter is the bandgap energy. The reflectance of the nanoparticles is required to rely upon few variables, for example, crystallite size of the nanoparticles, bandgap energy, lattice parameter, and oxygen inadequacy, structure of nanoparticles, surface unpleasantness and contamination centers. The optical band gap energy of the samples are investigated by Kubelka-Munk function (i.e., F(R) vs. photon energy graph). The reflectance spectrum reveals the Tauc's extrapolation equation as,

$$\alpha h\nu = A(h\nu\text{-}E_g)^n \qquad (2)$$

Where, α is absorption coefficient, h, the Plank's constant, A, a constant, ν, the photon energy, E_g, the bandgap energy, and the value of n denoted as $n = 1/2$ for direct bandgap and $n = 2$ for indirect bandgap of semiconductor materials [52]. The estimated bandgap values of the $Cd_xZn_{1\text{-}x}Fe_2O_4$ ($x = 0.0$, 0.1, 0.2, 0.3, 0.4 and 0.5) samples are 1.97, 1.92, 1.85, 1.83, 1.78, and 1.74 eV respectively. From Fig. 7, it is observed that the difference in bandgap energy and the crystallite size may be attributed to the

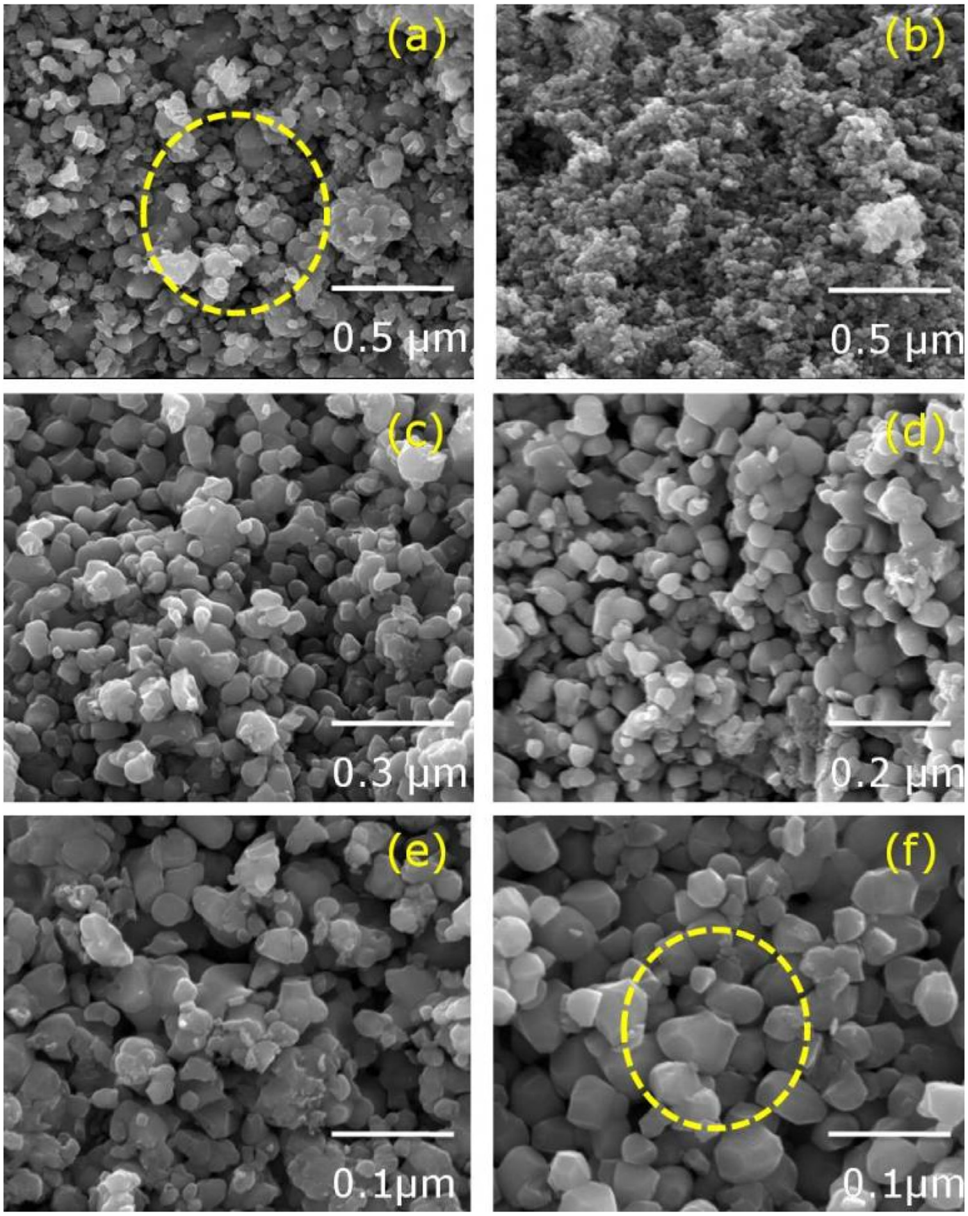

Fig. 6. Morphology of (a) Pure $ZnFe_2O_4$, (b) $Cd_{0.1}Zn_{0.9}Fe_2O_4$, (c) $Cd_{0.2}Zn_{0.8}Fe_2O_4$, (d) $Cd_{0.3}Zn_{0.7}Fe_2O_4$, (e) $Cd_{0.4}Zn_{0.6}Fe_2O_4$, (f) $Cd_{0.5}Zn_{0.5}Fe_2O_4$ nanoparticles using HR-SEM images.

increase in the doping concentration [53]. This result indicates that the pure zinc ferrite has strong absorptive power, but in the case of doped zinc ferrite, the absorptive power decreases. The values of bandgap energy are moderately lower in the doped samples and higher in pure samples, when compared to that of single crystalline bulk value (1.9 eV). It indicates that the particle size approaches to nano-regime, since the bandgap value decreases and also it could be clarified on the basis of increment in the lattice parameter with increasing dopant concentration. It might be due to the higher ionic radii of Cd^{2+} ions, when compared to Zn^{2+} ions [53]. The reduction in the bandgap energy may be attributed to the vacancies present in the intergranular regions, chemical defects, and interface imperfections in the agglomerated nanocrystals, and additional sub-bandgap energy that are affected by the abundant surface [54].

3.6. *Photoluminescence analysis*

The photoluminescence (PL) spectrum is an important tool to identify the optical and electronic properties of the synthesized semiconducting materials. It gives the information about the recombination phenomena and bandgap energy with

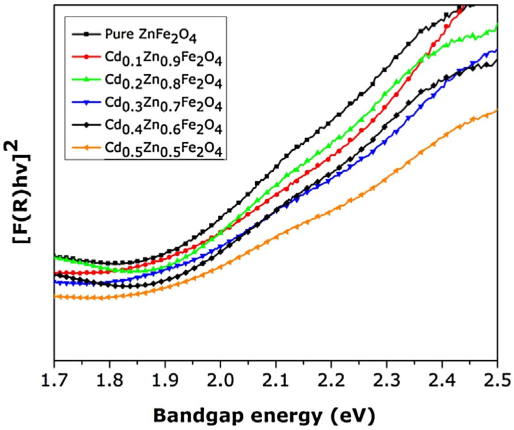

Fig. 7. Estimation of band gap energy of (a) Pure $ZnFe_2O_4$, (b) $Cd_{0.1}Zn_{0.9}Fe_2O_4$, (c) $Cd_{0.2}Zn_{0.8}Fe_2O_4$, (d) $Cd_{0.3}Zn_{0.7}Fe_2O_4$, (e) $Cd_{0.4}Zn_{0.6}Fe_2O_4$, (f) $Cd_{0.5}Zn_{0.5}Fe_2O_4$ nanoparticles using DRS studies.

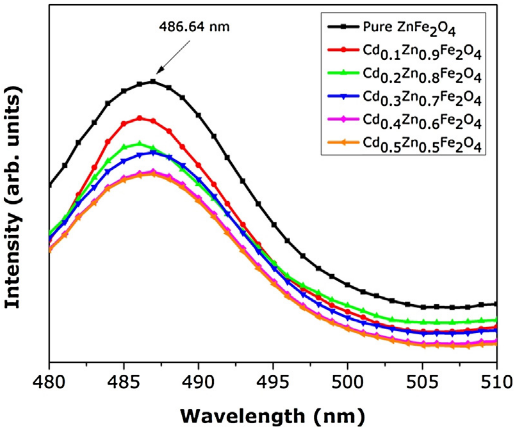

Fig. 8. Optical properties of (a) Pure $ZnFe_2O_4$, (b) $Cd_{0.1}Zn_{0.9}Fe_2O_4$, (c) $Cd_{0.2}Zn_{0.8}Fe_2O_4$, (d) $Cd_{0.3}Zn_{0.7}Fe_2O_4$, (e) $Cd_{0.4}Zn_{0.6}Fe_2O_4$, (f) $Cd_{0.5}Zn_{0.5}Fe_2O_4$ nanoparticles by using PL spectrum.

corresponding sub-bandgap deficiency states. The photoluminescence spectra are sensitive to the surface defects and it depends on the synthesis conditions, intensity of incident beam, dopant and its concentration, size and morphology of the samples and the excitation energy. The broadening of the spectra is mainly due to the particle size and particle size distribution. The crystallite size and surface defects of nanoparticles not only decrease the intensity of the peak but also influence the optical properties, such as bandgap energy. In the present study, Fig. 8 shows that the major peak present in the PL spectra for undoped and Cd^{2+} doped $ZnFe_2O_4$ (x = 0.0, 0.1, 0.2, 0.3, 0.4, 0.5 mol) around 486 nm that can be ascribed to blue emission [55]. The blue emission is attributed to the deep level visible region with localized levels in the bandgap energy. The excitation wavelength was fixed at 414 nm. When the Cd^{2+}content are increased, the intensity of emission peak is shifted to a lower wavelength, which could be due to a small variation in the Cd^{2+} distribution existing at the atomic scale. The intensity of emitted peak and the crystallite size decreases with an increase in the concentration of Cd^{2+} ions. Then, the maximum emission is shifted to lower energies, and is related to the quantum confinement effect [56].

3.7. Magnetization studies

Fig. 9(a–b) shows the distinctive magnetic properties recorded for the samples. The magnetic studies were carried out using vibrating sample magnetometer (VSM) and applied magnetic field (H_c) was plotted against saturation magnetization (M_s). It depends upon anisotropy, density, A-B exchange interactions and grain growth [57]. The values obtained from the magnetic curve are listed in Table 2. From this table, it is clear that the value of saturation magnetization for the pure samples is slightly greater than that of the doped samples. The decrease in the saturation magnetization in the doped sample might be due to the redistribution of cations (Cd^{2+}, Zn^{2+}) between the tetrahedral and octahedral sites [58]. The decrease in crystallinity and particle size with the decrease in the saturation magnetization is due to A-B super exchange interactions, and surface effects. The value of coercivity is increased by the increment in the Cd^{2+} content, which might be attributed to the Cd^{2+} ion replacement by Zn^{2+} ions. Cd^{2+} ions have the strong preference to occupy the octahedral site because magnetization

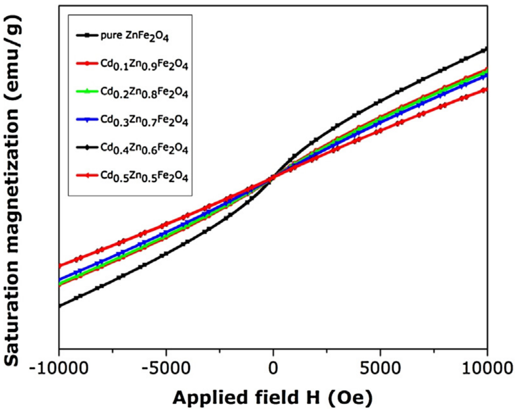

Fig. 9. Magnetic properties of (a) Pure $ZnFe_2O_4$, (b) $Cd_{0.1}Zn_{0.9}Fe_2O_4$, (c) $Cd_{0.2}Zn_{0.8}Fe_2O_4$, (d) $Cd_{0.3}Zn_{0.7}Fe_2O_4$, (e) $Cd_{0.4}Zn_{0.6}Fe_2O_4$, (f) $Cd_{0.5}Zn_{0.5}Fe_2O_4$ nanoparticles using RT magnetic spectrum.

Table 2
Magnetic parameters of pure and Cd^{2+} doped $ZnFe_2O_4$ nanoparticles.

Sample	Hc (Oe)	Mr(memu/g)	Ms (emu/g)
Pure $ZnFe_2O_4$	15.85	9.07	3.174
$Cd_{0.1}Zn_{0.9}Fe_2O_4$	16.42	7.097	2.251
$Cd_{0.2}Zn_{0.8}Fe_2O_4$	18.37	4.994	1.889
$Cd_{0.3}Zn_{0.7}Fe_2O_4$	19.38	4.798	1.857
$Cd_{0.4}Zn_{0.6}Fe_2O_4$	22.12	4.093	1.784
$Cd_{0.5}Zn_{0.5}Fe_2O_4$	22.15	4.063	1.546

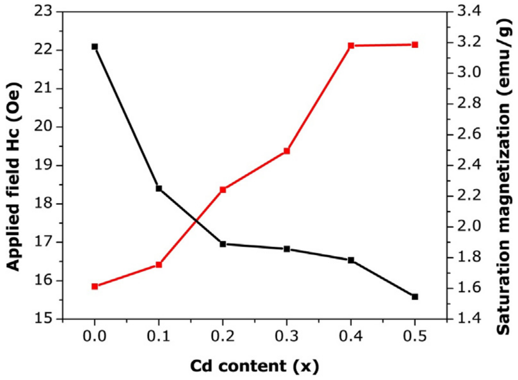

Fig. 10. Variation of applied magnetization and coercivity of (a) Pure $ZnFe_2O_4$, (b) $Cd_{0.1}Zn_{0.9}Fe_2O_4$, (c) $Cd_{0.2}Zn_{0.8}Fe_2O_4$, (d) $Cd_{0.3}Zn_{0.7}Fe_2O_4$, (e) $Cd_{0.4}Zn_{0.6}Fe_2O_4$, (f) $Cd_{0.5}Zn_{0.5}Fe_2O_4$ nanoparticles.

decreases and Cd^{2+} ion are non-magnetic (Fig. 10). There is a super exchange interaction occurring between the ions and the magnetic moment of the unit cell decreases with an increase in the concentration of Cd^{2+} ions. The low coercivity values obtained in the pure sample indicate that the sample is soft ferromagnetic in nature and can be demagnetized easily. The increase in coercivity might be due to the magnetocrystalline anisotropy and anisotropy exchange due to the spin disorder at the surface of the particles. The high coercivity and low saturation magnetization value obtained for the doped $ZnFe_2O_4$ samples is due to the presence of the defects in the crystalline lattice, and large magnetic anisotropy which inhibit the alignment of magnetic moment in the magnetic field [59].

4. Conclusions

The Cd^{2+} substituted zinc ferrite nanoparticles can be easily prepared via microwave assisted combustion method. The XRD pattern shows that pure zinc ferrite in single phase is formed. But the addition of Cd^{2+} gives rise to the formation of secondary phase due to the presence of α-Fe_2O_3. The lattice parameter increases with increasing cadmium substitution and obeys Vegard's law. The R-factor value decreases and is refined by Rietveld analysis. The results of FTIR spectra indicate the presence of metal oxide band in the sample. HRSEM images reveal that both the pure and the doped samples consist of almost spherical shape nanoparticles. The PL spectra of the samples are obtained at the excitation wavelength of 414 nm.

Finally, in the VSM analysis, the saturation magnetization decreases and the coercivity increases. With the addition of dopant Cd^{2+}, the value of crystallite size and saturation magnetization decreases and there is a considerable improvement in their structural, optical and magnetic properties.

Acknowledgement

We thank Loyola College management and the authors (MAM, AA) acknowledge the King Saud University, Deanship of Scientific Research, and College of Sciences, Research Center.

References

[1] M. Zheng, X.C. Wu, B.S. Zhou, Y.J. Wang, J. Magn. Magn. Mater. 183 (1998) 152–156.
[2] T. Prakash, G.V.M. Williams, J. Kennedy, S. Rubanov, J. Alloy. Compd. 667 (2016) 255–261.
[3] P.P. Murmu, J. Kennedy, B.J. Ruck, G.V.M. Williams, A. Markwitz, S. Rubanov, A.A. Suvorova, J. Mater. Sci. 47 (2012) 1119–1126.
[4] J. Kennedy, G.V.M. Williams, P.P. Murmu, B.J. Ruck, Phys. Rev. B 88 (2013) 214423.
[5] T. Prakash, G.V.M. Williams, J. Kennedy, S. Rubanov, J. Appl. Phys. 120 (2016) 123905.
[6] V.K. Sankaranarayanana, O. Prakasha, R.P. Panta, M. Islam, J. Magn. Magn. Mater. 252 (2002) 7–9.
[7] M. Arora, A. Kumar, R.P. Panta, Phys. Proc. 9 (2010) 20–23.
[8] J.J. Kingsley, K. Suresh, K.C. Patil, J. Mater. Sci. 25 (1990) 1305–1312.
[9] D.H. Chen, Y.Y. Chen, J. Colloid. Interface Sci. 235 (2001) 9–14.
[10] N.S. Chen, X.J. Yang, E.S. Liu, J.L. Huang, Sens. Actuators B: Chem. 66 (2000) 178–180.
[11] N. Rezlescu, C. Doroftei, E. Rezlescu, P.D. Popa, Sens. Actuators B: Chem. 115 (2006) 589–595.
[12] T. Tanaka, R. Shimazu, H. Nagai, M. Tada, T. Nakagawa, A. Sandhu, H. Handa, M. Abe, J. Magn. Magn. Mater. 321 (2009) 1417–1420.
[13] M. Shinkai, J. Biosci. Bioeng. 94 (2002) 606–613.
[14] A. Goldman, Modern Ferrite Technology, second ed., Springer, New York, 2006.
[15] R. Valenzuela, Magnetic Ceramics, Cambridge University Press, 1994.
[16] D. Carta, M.F. Casula, A. Falqui, D. Loche, G. Mount joy, C. Sangregorio, A. Corrias, J. Phys. Chem. C 113 (2009) 8606–8615.
[17] K. Krieble, M. Devlin, S.J. Lee, S.T. Aldini, J.E. Snyder, J. Appl. Phys. 103 (2008), 07E508-1-3.
[18] U. Hafeli, W. Schuut, J. Teller, M. Zborowski, Scientific and Clinical Applications of Magnetic Carriers, Plenum Press New York, 1997.
[19] Y. Koseoglu, A. Baykal, F. Gozuak, H. Kavas, Polyhedron 28 (2009) 2887–2892.
[20] C.N. Chinnasamy, M. Senoue, B. Jeyadevan, O. Perales-Perez, K. Shinoda, K. Tohji, J. Colloid Interface Sci. 263 (2003) 80–83.
[21] K.P. Chae, J. Lee, H.S. Kweon, Y.B. Lee, J. Magn. Magn. Mater. 283 (2004) 103–108.
[22] A. Ghasemi, S. Ekhlasi, M. Mousavinia, J. Magn. Magn. Mater. 354 (2014) 136–145.
[23] N. Kasapoglu, Synthesis, Characterization and ESR Studies of Magnetic Spinel Compounds, Master Thesis, Fatih University, Istanbul, 2008.
[24] C.C. Hwang, T.Y. Wu, J. Wan, J.S. Tsai, Mater. Sci. Eng. B 111 (2004) 49–56.
[25] L.C. Nehru, V. Swaminathan, C. Sanjeeviraja, Powder Technol. 226 (2012) 29–33.
[26] K. Kaviyarasu, E. Manikandan, J. Kennedy, M. Jayachandran, M. Maaza, Adv. Mater. Lett. 7 (2016) 684–696.
[27] K. Kaviyarasu, D. Sajan, M.S. Selvakumar, S.A. Thomas, D.P. Anand, J. Phys. Chem. Solids 73 (2012) 1396–1400.
[28] K. Kaviyarasu, E. Manikandan, P. Paulraj, S.B. Mohamed, J. Kennedy, J. Alloys Compd. 593 (2014) 67–70.
[29] K. Kaviyarasu, E. Manikandan, J. Kennedy, M. Maaza, RSC Adv. 5 (2015) 82421.
[30] K. Kaviyarasu, E. Manikandan, J. Kennedy, M. Jayachandran, Mater. Lett. 120 (2014) 243–245.
[31] K. Kaviyarasu, A. Ayeshamariam, E. Manikandan, J. Kennedy, R.L. Nandasivam, U.U. Gomes, M. Jayachandran, M. Maaza, Mater. Sci. Eng. B 210 (2016) 1–9.
[32] K. Kaviyarasu, E. Manikandan, J. Kennedy, M. Jayachandran, R.L. nandasiivam, U.U. Gomes, M. Maaza, Ceram. Int. (2017), http://dx.doi.org/10.1016/j.ceramint.2016.02.054 (Article in press).
[33] C. Karunakaran, A. Vijayabaalan, Mater. Sci. Forum 764 (2013) 206–218.
[34] B.E. Waren, X-ray Diffraction, Addison-Wesley, Reading, M.A, 1969.
[35] B.B. Dora, S. Kumar, M.C. Sahu, Int. J. Pharm. Sci. Rev. Res. 29 (2014) 307–311.
[36] C.N. Chinnasamy, A. Narayanasamy, N. Ponpandian, R.J. Joseyphus, K. Chattopadhyay, K. Shinoda, B. Jeyadevan, K. Tohji, K. Nakatsuka, H. Gueırault, J.M. Greneche, Scr. Mater. 44 (2001) 1411–1415.
[37] B. Gillot, D. Thiebaut, M. Laarj, Thermochim. Acta 342 (1999) 167–174.
[38] W. Kim, S.W. Hyun, T. Kouh, C.S. Kim, J. Korean Phys. Soc. 59 (2011) 3380–3384.
[39] O. Lupana, L. Chowa, G. Chaic, B. Roldana, A. Naitabdia, A. Schultea, H. Heinricha, Mater. Sci. Eng. B 145 (2007) 57–66.
[40] A.R. Denton, N.W. Ashcroft, Phys. Rev. A 43 (1991) 3161–3164.
[41] A. Goldman, Modem Ferrite Technology, 2nd edition, 1987, Pittsburgh, USA (ISBN 10: 0-387-29413-9).
[42] Y. Koseoglu, A. Baykal, F. Gozuak, H. Kavas, Polyhedron 28 (2009) 2887–2892.
[43] F. Gozuak, Y. Koseoglu, A. Baykal, H. Kavas, J. Magn. Magn. Mater. 321 (2009) 2170–2177.
[44] M. Gaudon, L.C. Robertson, E. Lataste, M. Duttine, M. Menetrier, D. Demourgues, Ceram. Int. 40 (2014) 5201–5207.
[45] O.M. Hemeda, M.M. Barakat, J. Magn. Magn. Mater. 223 (2001) 127–132.
[46] O.M. Lemine, M. Bououdina, M. Sajieddine, A.M. Al-Saie, M. Shafi, A. Khatab, M. Alhilali, M. Henini, Physica B 406 (2011) 1989–1994.
[47] H. Ehrhardta, S.J. Campbell, M. Hofmann, J. Alloys Compd. 339 (2002) 255–260.
[48] S. Hafner, Z. Kristallogr. 115 (1961) 331–358.
[49] R.D. Waldron, Phys. Rev. 99 (1955) 1727–1735.
[50] C.A. Ladole, Int. J. Chem. Sci. 10 (2012) 1230–1234.
[51] G.S. Li, L.P. Li, R.L. Smith, H. Inomata, J. Mol. Struct. 560 (2001) 87–90.
[52] S.F. Wang, F. Gu, M.K. Lu, X.F. Cheng, W.G. Zou, G.J. Zhou, S.M. Wang, Y.Y. Zhou, J. Alloys Compd. 394 (2005) 255–258.
[53] E.M.A. Jamal, D.S. Kumar, M.R. Anantharaman, Bull. Mater. Sci. 34 (2011) 251–259.
[54] S.K. Sampath, J.F. Cordaro, J. Am. Ceram. Soc. 81 (1998) 649–654.
[55] K. Kombaiah, J.J. Vijaya, L.J. Kennedy, M. Bououdina, Ceram. Int. 42 (2016) 2741–2749.
[56] E. Saion, N.M. Al- Hada, N. Soltani, P.J. Lee, Metals 5 (2015) 2383–2392.
[57] A. Kumar, M. Annveer, M.S. Arora, R.P. Yadav, Panta. Phys. Procedia 9 (2010) 20–23.
[58] J.F. Hochepied, M.P. Pileni, J. Appl. Phys. 87 (2000) 2472–2478.
[59] R.V. Magalaraja, S.A. kumar, P. Manohar, F.D. Gnanam, J. Magn. Magn. Mater. 253 (2002) 56–64.